NMR evidence of spinon localization in the kagome antiferromagnet $YCu_3(OH)_6Br_2[Br_{1-x}(OH)_x]$

Shuo Li,[1,*] Yi Cui [1,2,*] Zhenyuan Zeng,[3,*] Yue Wang,[1,*] Ze Hu,[1] Jie Liu,[1] Cong Li,[1] Xiaoyu Xu,[1] Ying Chen,[1] Zhengxin Liu,[1,2,†] Shiliang Li,[3,4,5,‡] and Weiqiang Yu [1,2,§]

[1]*Department of Physics and Beijing Key Laboratory of Opto-electronic Functional Materials and Micro-nano Devices,*
Renmin University of China, Beijing 100872, China
[2]*Key Laboratory of Quantum State Construction and Manipulation (Ministry of Education),*
Renmin University of China, Beijing 100872, China
[3]*Beijing National Laboratory for Condensed Matter Physics and Institute of Physics, Chinese Academy of Sciences, Beijing 100190, China*
[4]*School of Physical Sciences, University of Chinese Academy of Sciences, Beijing 100190, China*
[5]*Songshan Lake Materials Laboratory, Dongguan, Guangdong 523808, China*

We performed nuclear magnetic resonance studies on a kagome antiferromagnet $YCu_3(OH)_6Br_2[Br_{1-x}(OH)_x]$. No significant NMR spectral broadening is found in the Br center peak from 1 K down to 0.05 K, indicating absence of static antiferromagnetic ordering. In contrast to signatures of dominant 2D kagome antiferromagnetic fluctuations at temperature above 30 K, both the Knight shift K_n and the spin-lattice relaxation rate $1/T_1$ increase when the sample is cooled from 30 K to 8 K, which can be attributed to the scattering of spin excitations by strong nonmagnetic impurities. Unusually, a hump is observed in K_n and $1/T_2$ close to 2 K (far below the exchange energy), which indicates the existence of excitations with a large density of states close to zero energy. These phenomena are reproduced by a mean-field simulation of the Heisenberg model with bond-dependent exchange interactions, where the sign fluctuations in the spinon kinetic terms caused by impurities result in localization of spinons and an almost flat band close to the Fermi energy.

I. INTRODUCTION

Quantum spin liquids (QSLs) are an exotic phase of matter characterized by long-range quantum entanglement of spins with absence of long-range magnetic order [1–3]. Generally a QSL does not break any symmetry of the spin Hamiltonian and hosts fractional spinon excitations [4–6]. It was proposed that geometrical frustration in antiferromagnets can effectively enhance quantum fluctuations and suppress magnetic order. Therefore, QSL candidates have been extensively studied in antiferromagnets with triangular [7–10], kagome [11–15], and pyrochlore [16,17] lattices. Especially, the strongly frustrated spin-1/2 kagome Heisenberg antiferromagnet (KHAF) is considered as an ideal model to stabilize QSL ground states [13]. Theoretical works reveal that KHAF can exhibit no magnetic order even at zero temperature, but whether the ground state is gapped [18,19] or gapless [20–24] remains controversial.

However, most of the magnetic materials in nature exhibit long-range magnetic ordering at low temperatures, which makes it challenging to study QSL phases. On the experimental side, the mineral herbertsmithite $ZnCu_3(OH)_6Cl_2$ was thought to realize the ideal spin-1/2 KHAF model [11,13,25–29], in which Cu^{2+} ions with spin-1/2 moments arrange in structurally perfect kagome layers and nonmagnetic Zn^{2+} ions separate lattice planes to avoid 3D long-range antiferromagnetic (AFM) order. Accordingly, experiments on these materials are expected to provide a platform for determining spin excitations [11,13]. However, antisite randomness, that about 15% Cu^{2+} impurities occupy the nonmagnetic Zn^{2+} sites within the interlayers outside the kagome planes and 1% Zn^{2+} defects occupy the Cu^{2+} sites within the kagome planes, strongly affects the low-energy probes [11,13,27–32]. Bulk susceptibility χ is strongly enhanced by interlayer magnetic defects, preventing accurate measurements of intrinsic properties of the kagome layers [27,28]. It was further proposed that antisite randomness could disrupt QSL ground states [33]. Recent studies show that a certain fraction of Cu^{2+} spins forms robust QSL-like spin singlets with spatially varying gaps [29,33,34]. However, the fraction of spin singlets does not exceed 60% at $T \sim 0.01J$ and other Cu^{2+} spins remain paramagnetic [29]. Alternatively, the random singlet was also proposed as a candidate state in the 2D KHAF due to antisite randomness [35,36].

To avoid magnetic antisite disorder, Y-kapellasites $YCu_3(OH)_{6+x}Cl_{3-x}$ with $x = 0$, 1/3 have been synthesized. For $x = 0$, the compound exhibits AFM order at $T_N \approx 15$ K [37–40], which is partly attributed to a strong Dzyaloshinskii-Moriya (DM) interaction [41,42]. For $x = 1/3$, namely $Y_3Cu_9(OH)_{19}Cl_8$, with a distorted kagome lattice of Cu^{2+} which yields three different nearest-neighbor interactions, has a $T_N \approx 2.2$ K [40,42,43].

Recently, $YCu_3(OH)_6Br_2$ [$Br_{1-x}(OH)_x$] (YCu3-Br) was also synthesized and reported as a QSL candidate with no

---

*These authors contributed equally to this study.

†liuzxphys@ruc.edu.cn

‡slli@iphy.ac.cn

§wqyu_phy@ruc.edu.cn

magnetic ordering down to 2 K [44]. The material has perfect Cu^{2+} kagome planes with nearest exchange couplings $J \approx$ 79 K [44–48]. However, nonmagnetic antisite randomness among interlayer Br^- and OH^- exists because of their similar sizes [44–48]. In fact, recent studies indicate that substitution of OH^- for Br^- results in a nonsymmetrical Cu^{2+} hexagon in the kagome lattices, which leads to local distortions in the Cu-O-Cu exchange paths and therefore bond-dependent, nonuniform exchange couplings [47]. The impact of this type of antisite disorder to the ground state needs to be studied.

In this paper, we report ^{79}Br and ^{81}Br nuclear magnetic resonance (NMR) measurements on assembled high-quality single crystals of YCu_3-Br ($x = 0.67$). We found that the full width at half maximum (FWHM) of the NMR spectra barely changes with temperature from 1 K down to 50 mK. Combined with absence of magnetic ordering at higher temperatures by other studies, no static magnetic ordering in the system is concluded. Upon cooling to 30 K, the system is dominated by 2D KHAF physics as revealed by moderate increasing of the Knight shift K_n toward a peaked behavior. Below 30 K, Knight shift K_n, spin-lattice relaxation rate $1/T_1$, and spin-spin relaxation rate $1/T_2$ all increase upon cooling but with additive anisotropic and isotropic components, which suggests enhanced low-energy spin fluctuations from both interlayer couplings and disorder effects. A peak shows up below 2 K in both K_n and $1/T_2$, indicating that the spinons are scattered by nonmagnetic impurities and form a large amount of magnetic excitations with small but nonzero energy.

II. MATERIAL AND TECHNIQUES

Single crystals of YCu_3-Br ($x = 0.67$) were grown by the hydrothermal method as reported previously [46]. The lattice structure of YCu_3-Br is shown in Figs. 1(a) and 1(b), where Cu^{2+} ions form 2D kagome planes separated by Br^- layers. There are two inequivalent Br^- sites in the lattice, labeled as Br(1) and Br(2). The nonsymmetric distribution of OH^-/Br^- pushes 70% of Y^{3+} away from the ideal position, resulting in Y^{3+} occupancy probability of 35%, 30%, and 35%, from top to bottom.

For our NMR measurements, several crystals were aligned to a total size of $5 \times 6 \times 1.2$ mm^3, in order to improve the signal-to-noise ratio (see Sec. S6 in the Supplemental Material (SM) [49]). The samples were cooled in a variable-temperature insert for temperature above 2 K and a dilution refrigerator for temperature below 2 K. Spectra of ^{79}Br and ^{81}Br isotopes, having nuclear spin $I = 3/2$, Zeeman factor of $^{79}\gamma = 10.667$ MHz/T and $^{81}\gamma = 11.499$ MHz/T, and quadrupole moment of $^{79}Q = 0.33 \times 10^{-28}$ m^2 and $^{81}Q = 0.28 \times 10^{-28}$ m^2, respectively, were collected with the standard spin-echo sequences $\pi/2$-τ-π where time length of the $\pi/2$ pulse is about 2 μs. The full NMR spectra are obtained by integrating spin-echo spectra with field sweeping at fixed frequencies.

We primarily study the spin fluctuations on the Br(1) site, because the spectral weight of Br(2) is expected to be 1/6 of that of Br(1), following their occupancy ratios in the lattice. The Knight shift K_n is calculated by the form $K_n = (f - f_\nu)/\gamma H - 1$, where f is peak frequency in the spectrum, f_ν is the frequency correction due to quadrupole
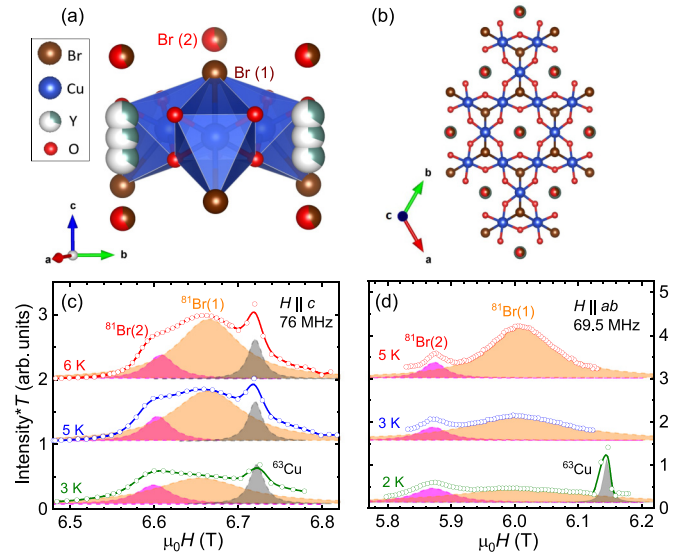

FIG. 1. Crystal structure and presentative spectra of YCu_3-Br. (a) Side view of the crystal structure, in which hydrogens are not shown. (b) Top view of the kagome plane. Cu^{2+} atoms are surrounded by O atoms and Br atoms. Two inequivalent Br sites are shown, with Br(1) above and below the center of Cu^{2+} triangles and Br(2) located at the interlayer which is partly occupied by OH^-. Y atoms reside on three positions (cyan) with the occupancy ratio of 35%, 30%, and 35%, respectively. (c) Br spectra measured with $H||c$ at a fixed frequency 76 MHz. $^{81}Br(1)$ and $^{81}Br(2)$ spectra partly overlap with ^{63}Cu spectra (gray) from the NMR coil. (d) Br spectra measured with $H||ab$ at a fixed frequency 69.5 MHz, also partially overlapping with environmental ^{63}Cu spectra as labeled.

moment contributions, and H is external field. The spin-lattice relaxation rate $1/T_1$ was measured by inversion-recovery method, by fitting nuclear magnetization to the standard recovery function for spin-3/2 isotopes, $M(t) = M_0[1 - 0.1e^{-(t/T_1)^\beta} - 0.9e^{-(6t/T_1)^\beta}]$, where β is the stretching factor. The spin-spin relaxation rate $1/T_2$ was obtained by fitting the transverse spin recovery with Lorentz form, that is, $M(t) = M_0[0.1e^{-(t/T_2)^\beta} + 0.9e^{-(6t/T_2)^\beta}]$. The detailed spin recovery curves and the fittings are presented in Sec. S6 of the SM [49].

III. NMR SPECTRA

We performed ^{79}Br and ^{81}Br NMR measurements at different frequencies. Typical spectra are partly demonstrated in Figs. 1(c)–1(d) and Fig. 2(a), and full spectra in Fig. 3(a), with different field orientations and field ranges. In principle, twelve NMR lines are expected in each full spectrum, considering two inequivalent sites and two types of spin-3/2 Br isotopes. Each type of isotope produces one center transition and two satellite transition lines in the spectrum at a constant field, due to hyperfine field from Cu^{2+}, and coupling among the nuclear quadrupole moments and the local electric field gradient (EFG).

Due to antisite disorder, the change of O^{2-} position in Cu-O-Cu bond results in the variation in both the EFG and the hyperfine field on the Br sites, which broadens the Br NMR spectra by both a quadrupolar and a magnetic effect as observed in this study.
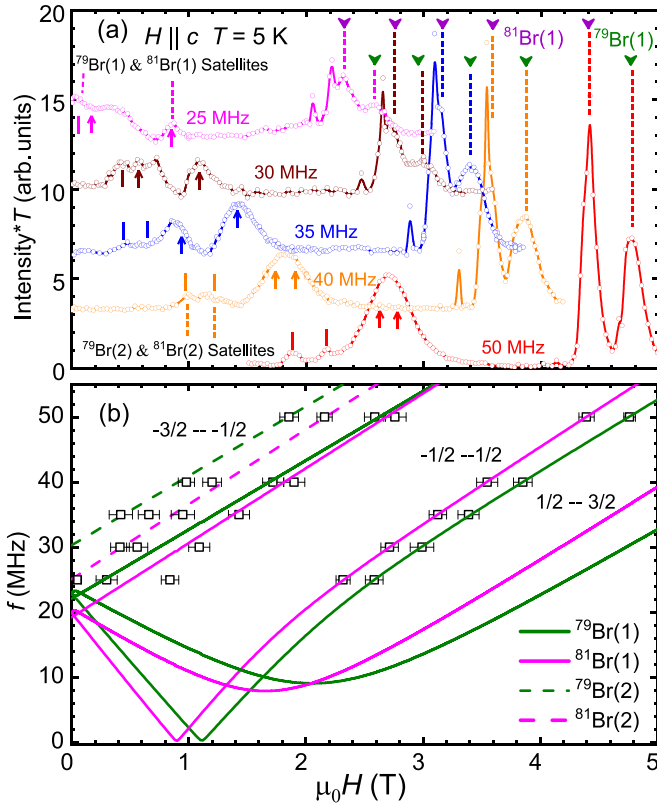
FIG. 2. Br spectra at 5 K with $H \| c$. (a) Br NMR spectra measured with fixed frequencies as functions of fields. Vertical offsets are applied for clarity. The downward arrows mark the locations of the Br(1) central peaks, and the upward arrows mark the Br(1) satellite peaks. The vertical solid lines represent the satellites of Br(2). (b) Peak frequencies of the spectra as functions of fields. The solid lines are fit to the resonance frequencies, from contributions of different nuclear sites and isotopes as labeled (see text). Corresponding assignments of spectra to isotopes are also labeled in panel (a).

The frequencies of observed resonance peaks are then plotted in Fig. 2(b) as functions of fields, which can be assigned to different sites and isotopes, following three conditions. First, the relative spectral weight of Br(2) and Br(1) should follow a ratio of 1:6 as described in Sec. II. Second, the hyperfine shift of Br(2) should be smaller compared to that of Br(1), because of its larger distance to magnetic Cu^{2+} ions. Third, ^{79}Br has a smaller Zeeman factor and a larger quadrupole moment compared to ^{81}Br, which results in a smaller resonance frequency for ^{79}Br center peaks but a larger quadrupole correction for satellite peaks. By reading the frequency at the spectral of NMR and NQR spectra, the peak frequencies of the spectrum can be fitted with parameters $^{79}\nu_Q(1) = 24.3$ MHz, $^{81}\nu_Q(1) = 21.5$ MHz, $^{79}\nu_Q(2) = 30.3$ MHz, and $^{81}\nu_Q(2) = 25.09$ MHz, which are demonstrated by the fit curves of resonance frequencies in Fig. 2(b). The detailed fitting procedure is included in the SM [49]. The fit curves of the solid and dotted lines are in good consistency with the experimental data. Then all the resonance peaks are assigned to different Br sites and isotopes as labeled in Figs. 1(c)–1(d) and Fig. 2(a).

Figure 3(a) presents full Br spectra from 5 K to 50 mK. To reduce spectral overlaps among different transition lines,

different parts of the Br(1) spectra are then measured with selected frequencies at three temperature ranges, that is, from 5 K to 170 K on center transitions [Fig. 3(b)], from 1.5 K to 15 K on satellites [Fig. 3(c)], and from 50 mK to 1 K on center transitions [Fig. 3(d)]. The FWHM of the ^{79}Br(1) spectra [Fig. 3(d)] is obtained by Lorentz fitting and shown in Fig. 4.

Upon cooling, the NMR spectra show a progressive broadening with temperatures from 8 K to 1.5 K. However, no further line broadening is observed with temperatures from 1 K down to 50 mK, and the NMR linewidth tends to saturate below 1 K (Fig. 4). In a previous report, the neutron scattering data exhibit no long-range magnetic order down to 0.3 K [50]. Combining these two pieces of information, our data provide evidence for absence of static antiferromagnetic ordering in YCu₃-Br with temperature down to 50 mK.

IV. NMR KNIGHT SHIFT

To reveal spin fluctuations of the system, the Knight shift K_n, deduced from the Br(1) spectra shown in Figs. 3(b)–3(d), is plotted as functions of temperatures in Fig. 5(a). Note that K_n is determined by the frequency at the peak position of the spectra, and the error bar is calculated by $\Delta f / \gamma H$, where Δf is the frequency difference between the actual peak and the fitted peak (data not shown) in the spectra. Upon cooling below 200 K, K_n first exhibits a slow increase with a shoulder behavior between 30 K and 15 K, then undergoes a rapid raise from 8 K to 0.8 K, and finally decreases after reaching a peak at about 0.5 K. The temperature dependence of $K_n(T)$ is consistent with the bulk susceptibility $\chi(T)$ (adapted data from Ref. [46]) down to 0.5 K, as shown in Fig. 5(b). Together with the extremely low temperature data, K_n reveals important information of the spin excitations at different energy scales [13,27,29].

Generally, $K_n = K_s + K_{orb}$, where K_{orb} is the orbital contribution to Knight shift which does not change with temperature, and $K_s(T)$ is the spin contribution. Note that $K_s(T) = A_{hf}\chi(T)/N_A\mu_B$, where $\chi(T)$ is the bulk spin susceptibility, A_{hf} is the magnetic hyperfine coupling constant, and N_A is Avogadro's number. The high-temperature $K_n(T)$ is then plotted against $\chi(T)$ as shown in the inset of Fig. 5(a), where it follows a straight line and gives the hyperfine coupling $A_{hf} = -4.74 \pm 0.14$ kOe/μ_B. K_{orb} of -0.0448% is determined by the intercept with the y axis at $\chi = 0$.

It was proposed theoretically that $\chi(T)$ in the 2D KHAF yields a peak at temperature on the order of $T \sim 0.15J$ [24]. The shoulder behavior in both $K_n(T)$ and $\chi(T)$ between 15 K and 30 K indicates that the low-energy spin dynamics above 30 K in this system is dominated by the intrinsic behavior of the 2D KHAF, given that $J \approx 79$ K [45,46].

Below 15 K, however, the absence of the rapid drop in $K_n(T)$ and $\chi(T)$ indicates that another mechanism exists. Indeed, K_n shows a remarkable upturn with decreasing temperature and reaches a peak at around 0.5 K. At first glance, the peak at 0.5 K may be caused by a criticality toward 3D ordering owing to 3D interlayer coupling. However, with such a high onset temperature of upturn, a very strong interlayer coupling has to be considered, which is contradictory with the absence of 3D long-range ordering as reported in Sec. III. An alternative interpretation for the peak is that there exists
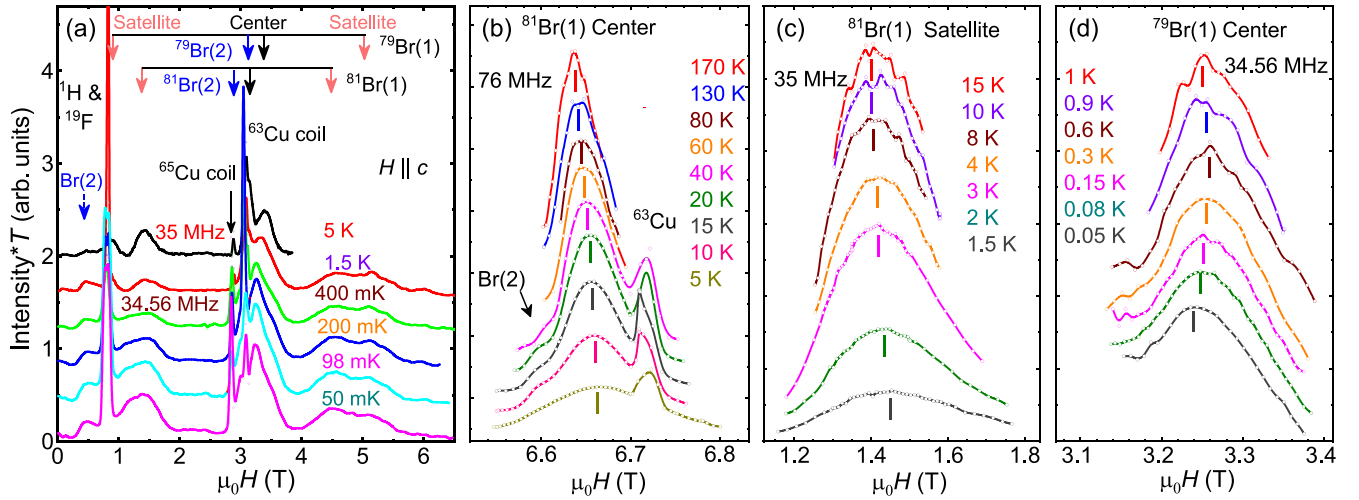
FIG. 3. Br Spectra at different temperatures with $H||c$. (a) Presentative full spectra acquired as functions of fields, with center and satellite transition lines of Br(1) and Br(2) specified. ^{1}H, ^{19}F, and ^{63}Cu note the environmental NMR signals. (b)–(d) ^{81}Br(1) lines at high, intermediate, and low temperatures, respectively. Vertical lines mark the peak positions.

a large density of low-energy magnetic excitations caused by nonmagnetic impurities as discussed below.

We preformed theoretical simulations of the 2D kagome Heisenberg model with bond-dependent interactions using fermionic spinon mean-field theory. Considering that the ground state has no magnetic order, the spinon representation, with an unbroken rotational symmetry, is convenient to describe the magnetic disorder ground state in the mean-field approach. Under a local constraint $\sum_{\sigma} f_{i\sigma}^{\dagger} f_{i\sigma} = 1$, the exchange interaction is rewritten as $J_{ij} S_i \cdot S_j = -\frac{J_{ij}}{2} \sum_{\alpha\beta} f_{i\alpha}^{\dagger} f_{j\alpha} f_{j\beta}^{\dagger} f_{i\beta}$. Under the mean-field approximation, the spin-spin interactions are decoupled into the noninteracting trial Hamiltonian $H_{\mathrm{MF}} = \sum_{ij,\sigma} \eta_{ij} (t_{ij} + \delta_{ij}) f_{i\sigma}^{+} f_{j\sigma} + \mathrm{H.c.} + \lambda \sum_i f_{i\sigma}^{\dagger} f_{i\sigma}$, where $f_{\uparrow}$ and $f_{\downarrow}$ are fermionic spinon

operators, σ is the spin index, t_{ij} is the averaged hopping amplitude (the kinetic term) for the spinons, δ_{ij} is amplitude fluctuations in the hopping, η_{ij} represents phase randomness in the hopping, and λ is the Lagrangian multiplier for the constraint $\sum_{\sigma} f_{i\sigma}^{\dagger} f_{i\sigma} = 1$. We emphasize that nonuniform exchange interactions J_{ij} are the physical origin of phase fluctuations η_{ij} and amplitude fluctuations δ_{ij} in the spinon kinetic energy term.

In the simulations, we first assume that the amplitude fluctuations δ_{ij} obey Gaussian distribution. However, the amplitude fluctuations only moderately change the ground state
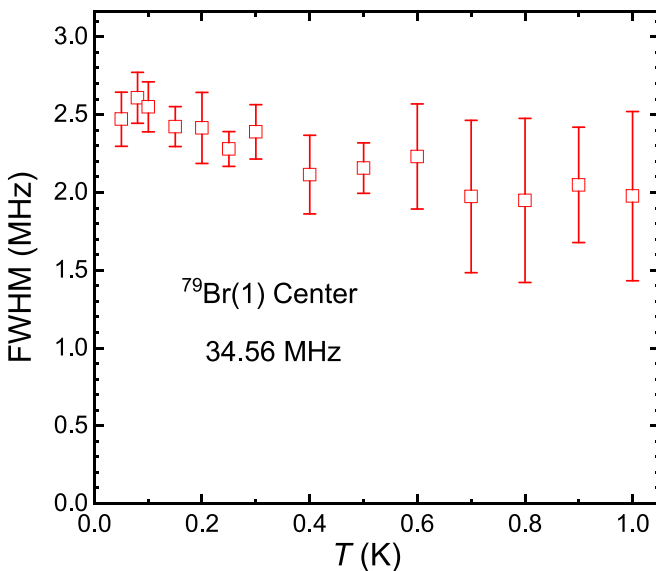

FIG. 4. Low-temperature FWHM of the spectra. The FWHM with temperature from 1 K to 50 mK, with $H||c$, obtained from Fig. 3(d).
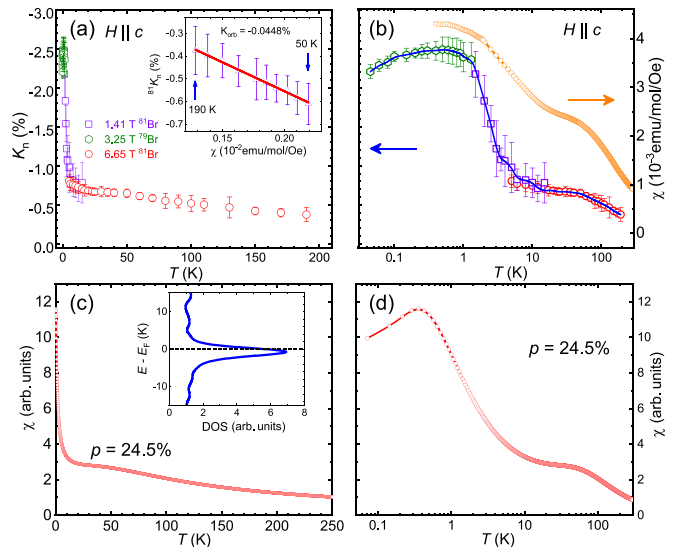

FIG. 5. Experimental Knight shift, and theoretical bulk susceptibility by a mean-field calculation. (a) K_n as functions of temperatures measured with different fields. Inset: $^{81}K_n$ vs χ with temperatures from 50 K to 190 K. (b) K_n (left) and χ (right) adapted from Ref. [46] of the crystals in a semilog scale. (c) χ as a function of temperatures, calculated based on QSL state with spinon Fermi surface and bond disorder $p = 24.5\%$ (see text). Inset: Density of states as a function of energy. (d) Semilog plot of χ as a function of temperatures.

(see SM [49]). Then we turn on the phase fluctuations η_{ij} and simply consider them as random sign distributions due to the unbroken time reversal symmetry, namely, $\eta_{ij} = \pm 1$ with probability $P(-1) = p$ and $P(1) = 1 - p$. It turns out that sign fluctuations strongly affect the nature of the ground state. No matter what the initial state is, a Dirac cone state or a spinon Fermi surface state, as the probability of sign flips reaches a threshold $p = 17\%$, an almost flat band with large density of states appears at energy around zero, as shown in the inset of Fig. 5(c). The original flat band(s) of the unperturbed kagome lattice locating at the top of the spinon band structure disappear due to impurities. Furthermore, with such probability of sign flips, the motion of spinons will be suppressed due to the destructive interference effect. As a result, all the spinon eigenstates are localized in the lattice space [49]. Since the spinons are quasiparticles in strongly interacting systems, the suppression of spinon motion is essentially many-body localization. A similar mechanism also occurs in the charge localization in doped Mott insulators [51,52]. Within this theoretical scenario, the bulk magnetic susceptibility χ is then calculated and shown in Figs. 5(c) and 5(d). The low-energy (nearly) flat band resulting from the phase randomness gives rise to a prominent upturn in χ at $T \leqslant 0.101J$ and a peak at about $T = 0.0063J$, followed by a drop at even lower temperatures.

The above theoretical results of χ are in good consistency with the experimental data of K_n in respect to their overall shape and their characteristic temperatures. Taking $J \approx 79$ K [46], then the shoulder appears at around $0.51J \sim 40$ K and the upturn starts at around $0.101J \sim 8$ K, which is in perfect agreement with the Knight shift data in Fig. 5(b). At the extremely low temperature region, a peak shows up at 0.5 K, which is slightly lower than that of K_n. The appearance of the peak is due to the large density of states of the almost flat band with very low but nonzero energy [see the inset of Fig. 5(c)]. We calculated the fraction of the integrated weight of spinons in the flat band, and found that 6.3% spinons are sufficient to account for the observed upturn in the calculated χ. The peaked behavior, observed in K_n, shown at temperatures below 1.5 K, is consistent with the flat band picture. This is in contrast to a Curie-Weiss behavior as expected for magnetic impurity effect.

Therefore, the large resemblance in the temperature dependence of the experimental data [Fig. 5(a)] and the theoretical results [Fig. 5(c)], in a rather large temperature range, supports that our measured K_n is strongly affected by disordered fermionic excitations rather than 3D couplings. Besides, the shouldered behavior in the specific heat data, calculated from the flat band around the Fermi surface [49], also agrees well with experiment [46].

V. SPIN-LATTICE RELAXATION RATE

The spin-lattice relaxation rate $1/T_1$ is a sensitive probe of low-energy fluctuations. In Fig. 6(a), $1/T_1$ for ^{81}Br(1) is shown as a function of temperature. $1/T_1$ increases with temperature from 40 K to 200 K, which should be a signature of AFM fluctuations. Data at typical field below 3 K are not presented, where the stretching factor $\beta \leqslant 0.6$ and therefore $1/T_1$ data are not reliable. Below 1.5 K, the longitudinal spin
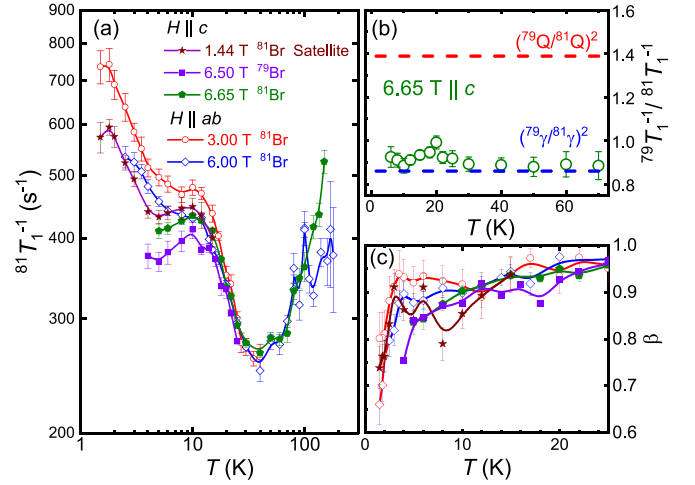

FIG. 6. Spin-lattice relaxation rate. (a) $1/T_1$ as functions of temperatures, measured on the center and satellite lines of ^{81}Br(1) at different fields. (b) Ratios of $1/T_1$ on two types of isotopes, measured at 6.65 T. The horizontal lines mark the values of $(^{79}Q/^{81}Q)^2$ and $(^{79}\gamma/^{81}\gamma)^2$, respectively. (c) Stretch factors β for fitting the spin-recovery curve.

recovery (data not shown) exhibits a two-exponent behavior for unclear reasons, which prevents us from making further studies on $1/T_1$ at lower temperature.

For nuclei with quadruple moments, $1/T_1$ is contributed by both magnetic fluctuations and lattice fluctuations through couplings to the local hyperfine fields and EFGs, respectively. Thanks to different Zeeman factors and quadrupole moments of ^{79}Br and ^{81}Br, these two contributions can be identified, as the spin fluctuation part is proportional to γ_n^2 and the lattice fluctuation part is proportional to Q^2. For example, the spin contribution to $1/T_1$ is written as $1/T_1 = \gamma_n^2 k_B T / \mu_B^2 \sum_q A_{hf}^2(q) \text{Im} \frac{\chi(q,\omega)}{\omega}$, where $\chi(q,\omega)$ is the dynamical susceptibility, ω is the Larmor frequency of the nuclei, and A_{hf} is the hyperfine coupling constant.

In Fig. 6(b), the ratio of $1/^{79}T_1$ and $1/^{81}T_1$ is plotted as a function of temperature. Two horizontal lines, with constant values of $(^{79}\gamma/^{81}\gamma)^2 = 0.861$ and $(^{79}Q/^{81}Q)^2 = 1.389$, are added as references which set the limit for pure magnetic and pure structural fluctuation cases, respectively. For temperatures from 8 K to 70 K, $^{79}T_1^{-1}/^{81}T_1^{-1}$ falls close to the lower line, which indicates that magnetic fluctuations dominate in $1/T_1$ at temperatures below 70 K, whereas no structural fluctuations are found. Therefore, we can conclude that there is no structural instability from 70 K down to 5 K.

With temperatures below 30 K, $1/T_1$ shows a prominent upturn upon cooling, which suggests the development of low-energy spin fluctuations. Furthermore, $1/T_1$ does not change with field values and orientations until below 15 K, which suggests that the spin fluctuations at temperatures between 15 K and 30 K are very isotropic. The large onset temperature of the spin fluctuations and its isotropic behavior may not be described by the 3D AFM fluctuations induced by interlayer couplings, for the following two reasons. First, the 3D AFM fluctuations in the lattice are usually anisotropic. Second, the energy scale of the interlayer coupling is about 2.4 K [44,45], which is too small to account for such a high onset
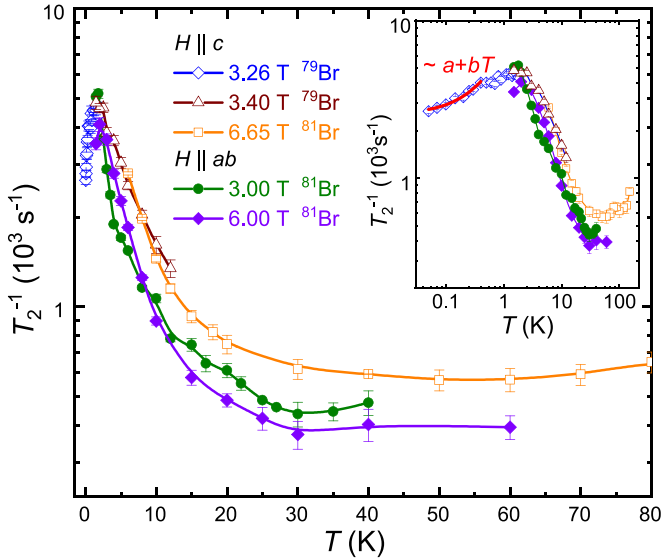
FIG. 7. Spin-spin relaxation rate. $1/T_2$ as functions of temperatures measured with different fields. Inset: log-log plot of $1/T_2$. The solid line represents a linear fit of $a + bT$ to the low-temperature data.

temperature of upturn. In particular, the antisite disorder on the Br(2) sites, which sets in between the Cu^{2+} layers, may further reduce the 3D couplings. On the contrary, nonmagnetic impurities, as described in Sec. IV, may lead to such enhancement of isotropic spin fluctuation at $T \leqslant J/2$, as observed by the temperature dependence of K_n and χ [Figs. 5(a)–5(d)].

Below 8 K, however, $1/T_1$ exhibits an upturn with $H||ab$, but a downtown with $H||c$, and $1/T_1$ is also reduced with field in both orientations below 1.8 K. The dramatic anisotropic and the field-suppression effects in $1/T_1$ may result from the development of anisotropic AFM fluctuations due to interlayer couplings and spin-orbit coupling such as the Dzyaloshinskii-Moriya (DM) interactions, with the easy axis along the c axis. $1/T_1$ increases when cooled from 5 K to 1.8 K with an upturn at low temperature, which in principle should indicate gapless excitations which will be further discussed with the $1/T_2$ data. In fact, the linewidth of Br(1) spectra, as shown in Fig. 3(c), also increases dramatically below 8 K, which is consistent with the development of short-range correlations, though the ordering tendency is suppressed by the inherent antisite disorder in the system. In this temperature range, disorder-induced spin fluctuations, though prominent as shown in χ [Fig. 5(b)], may overlap with the 3D anisotropic fluctuations as discussed above. The $1/T_2$, on the other hand, reveals dominant isotropic spin fluctuations as shown in the following section.

VI. SPIN-SPIN RELAXATION RATE

To further study the low-energy spin dynamics, the spin-spin relaxation rate $1/T_2$ was measured. The detailed data with different field values and orientations are shown in Fig. 7(a). Compared to the $1/T_1$ data, the overall trend of $1/T_2$ with temperature seems to be similar, where a dip forms at about 30 K, followed by an upturn upon cooling. However, there are also distinctive behaviors in the $1/T_2$.

First, the stretching factor β remains as one in the whole temperature range, by fitting transverse spin recovery to obtain T_2, as described in Sec. II. Therefore, $1/T_2$ reveals intrinsic behavior of the compound.

Second, from 30 K to 2 K, no kinked behavior is found in the log-log plot of $1/T_2(T)$ (Fig. 7 inset). In particular, at temperatures below 8 K, the changes of $1/T_2$ with field orientations and field amplitudes are very small, which suggests that $1/T_2$ is dominated by isotropic spin fluctuations in the whole temperature range, compared to the anisotropic fluctuations in $1/T_1$ below 8 K. This suggests that dominant fluctuation revealed by $1/T_2$ should be affected by another mechanism rather than 3D coupling effects. In fact, the scattered spinons, as discussed in Sec. IV, can account for such upturn in a large temperature range below $T \leqslant J/2$, by enhanced low-energy spin fluctuations from the flat band, from the spinon Hamiltonian with phase randomness discussed in Sec. IV.

Lastly, a remarkable peak develops in $1/T_2$ at about 1.5 K, below which $1/T_2$ decreases dramatically. In this aspect, $1/T_2$ behaves very similarly to K_n by showing a peaked behavior, albeit at a slightly higher temperature. These observations are all aligned with the flat band of scattered spinons at a finite energy of $0.0063J$ (Sec. IV). The different peak temperatures in K_n and $1/T_2$ may be related to a shorter timescale for measurements of $1/T_2$.

We attempted to fit $1/T_2$ by the form $1/T_2 = a + bT$, at temperatures between 50 mK and 400 mK. As shown by the solid line in the inset of Fig. 7, the success of the fitting suggests additive contributions to $1/T_2$: a constant term and a linear-T term. In principle the linear-T term presents gapless excitations with a Fermi surface, which may be caused by a Fermi-surface-like behavior at high temperatures, by picking up the peaked spectra at finite energies as shown in Fig. 5(c) (inset).

VII. DISCUSSION

In YCu$_3$-Br, the behavior of K_n, $1/T_1$, and $1/T_2$ at all temperatures can be accounted for by antisite randomness, 3D spin fluctuations (resulting from interlayer coupling), and DM interactions. Note that only $1/T_1$ shows anisotropic spin fluctuations which should be caused by the interlayer couplings and DM interactions. We also note that the external field suppresses the anisotropic short-ranged AFM correlations as revealed by $1/T_1$, which may help to stabilize a QSL ground state as revealed by a recent work [53], and deserves further study.

Our study suggests that nonmagnetic antisite randomness seems to be crucial in 2D KHAF. On one hand, DM interactions, which give rise to AFM long-range order in YCu$_3$(OH)$_6$Cl$_3$ [38,54,55], are suppressed by strong disorder in YCu$_3$-Br. On the other hand, the antisite disorder between Br(2) and OH$^-$ and Y atom displacement may cause bond randomness, namely, fluctuating exchange couplings in the Cu-O-Cu path [45] within a finite energy range around J. In our mean-field model, this fluctuation in exchange couplings may change the ground state of this system.

At the mean-field level, the randomness in the bond interactions can cause both amplitude fluctuations and phase fluctuations of the spinon kinetic terms. If the phase

randomness p reaches 17%, on top of a Fermi-surface-like density of states, the spinon dispersion has an almost flat band close to the Fermi energy. The physical responses of the low-energy flat band agree well with the experimental data, including the linear temperature dependence in $1/T_2$ and the sharp peak in K_n at 0.5 K. The nearly flat energy band corresponds to low-energy spinons excitations which are spatially localized. The existence of large density of states close to zero energy is quite different from the picture of random singlet states [35,36].

Interestingly, besides the spinons in the nearly flat band, almost all of the spinon eigenstates are localized in lattice space, as shown in the SM [49]. Since the spinons are collective excitations resulting from strong interactions, the localization of spinons is essentially many-body localization caused by the randomness in the interaction strength. The localized spinons contribute to both specific heat and susceptibility, but not to the thermal transport. As a by-product, our work indicates that the thermal conductance of YCu$_3$-Br contributed by the spinons is very small [48]. Localized magnons are not considered since there is no evidence of long-range magnetic order in the system.

It is enlightening to compare the localized spinons with isolated magnetic impurities despite that our sample is of high quality. Here we list several essential differences. First, the density of impurities is generally very small, but the localized spinons have a flat band at low energy which has a very large density of states. Second, the localization of spinons results from strong spin-spin interactions, and as a result the localized spinons interact with each other via internal gauge fields (and hence have stronger quantum fluctuations). On the other hand, the isolated magnetic impurities weakly interact with each other. Third, the localized spinons obey fractional (fermionic) statistics while the energy of isolated impurities obeys the Bose distribution (or approximately Boltzmann distribution since the density is very low). Consequently, the magnetic

susceptibility (and Knight shift) of the latter obey the Curie law but that of the former deviates from the Curie law due to the fermionic statistics. For simplicity, we did not include possible DM interactions in the theoretical simulations.

VIII. SUMMARY

In summary, our study provides spectroscopic evidence for the absence of AFM ordering in YCu$_3$-Br with temperatures down to 50 mK. The K_n, $1/T_1$, and $1/T_2$ data at temperatures above 30 K reveal intrinsic behavior of the 2D KHAF, unaffected by disorder. The effect of the site-randomness disorder leads to enhanced low-energy spin fluctuations below 30 K, consistent with our mean-field calculation of magnetic susceptibility, by considering amplitude and sign randomness in the spinon kinetic term which give rise to a Fermi-surface-like band structure. In particular, both K_n and $1/T_2$ are peaked at very low temperatures, which are consistent with the peak in the spinon density of states contributed from the nearly flat band close to zero energy. Our results suggest that nonmagnetic site disorder has a significant impact on the spinon dispersion in the $S = 1/2$ KHAF system and may cause many-body localization.

[1] L. Balents, Spin liquids in frustrated magnets, Nature (London) **464**, 199 (2010).

[2] Y. Zhou, K. Kanoda, and T. K. Ng, Quantum spin liquid states, Rev. Mod. Phys. **89**, 025003 (2017).

[3] C. Broholm, R. J. Cava, S. A. Kivelson, D. G. Nocera, M. R. Norman, and T. Senthil, Quantum spin liquids, Science **367**, eaay0668 (2020).

[4] S. A. Kivelson, D. S. Rokhsar, and J. P. Sethna, Topology of the resonating valence-bond state: Solitons and high-T_c superconductivity, Phys. Rev. B **35**, 8865 (1987).

[5] N. Read and B. Chakraborty, Statistics of the excitations of the resonating-valence-bond state, Phys. Rev. B **40**, 7133 (1989).

[6] X. G. Wen, Mean-field theory of spin-liquid states with finite energy gap and topological orders, Phys. Rev. B **44**, 2664 (1991).

[7] Y. Shimizu, K. Miyagawa, K. Kanoda, M. Maesato, and G. Saito, Spin liquid state in an organic Mott insulator with a triangular lattice, Phys. Rev. Lett. **91**, 107001 (2003).

[8] T. Isono, H. Kamo, A. Ueda, K. Takahashi, M. Kimata, H. Tajima, S. Tsuchiya, T. Terashima, S. Uji, and H. Mori, Gapless quantum spin liquid in an organic spin-1/2 triangular-

lattice κ-H$_3$(Cat-EDT-TTF)$_2$, Phys. Rev. Lett. **112**, 177201 (2014).

[9] Y. Shimizu, T. Hiramatsu, M. Maesato, A. Otsuka, H. Yamochi, A. Ono, M. Itoh, M. Yoshida, M. Takigawa, Y. Yoshida, and G. Saito, Pressure-tuned exchange coupling of a quantum spin liquid in the molecular triangular lattice κ-(ET)$_2$Ag$_2$(CN)$_3$, Phys. Rev. Lett. **117**, 107203 (2016).

[10] Y. S. Li, D. Adroja, R. I. Bewley, D. Voneshen, A. A. Tsirlin, P. Gegenwart, and Q. M. Zhang, Crystalline electric-field randomness in the triangular lattice spin-liquid YbMgGaO$_4$, Phys. Rev. Lett. **118**, 107202 (2017).

[11] T. H. Han, J. S. Helton, S. Y. Chu, D. G. Nocera, J. A. Rodriguez-Rivera, C. Broholm, and Y. S. Lee, Fractionalized excitations in the spin-liquid state of a kagome-lattice antiferromagnet, Nature (London) **492**, 406 (2012).

[12] T. H. Han, J. Singleton, and J. A. Schlueter, Barlowite: A spin-1/2 antiferromagnet with a geometrically perfect kagome motif, Phys. Rev. Lett. **113**, 227203 (2014).

[13] M. X. Fu, T. Imai, T. H. Han, and Y. S. Lee, Evidence for a gapped spin-liquid ground state in a kagome Heisenberg antiferromagnet, Science **350**, 655 (2015).

[14] M. R. Norman, *Colloquium*: Herbertsmithite and the search for the quantum spin liquid, Rev. Mod. Phys. **88**, 041002 (2016).

[15] P. Puphal, K. M. Zoch, J. Désor, M. Bolte, and C. Krellner, Kagome quantum spin systems in the atacamite family, Phys. Rev. Mater. **2**, 063402 (2018).

[16] M. J. Harris, S. T. Bramwell, D. F. McMorrow, T. Zeiske, and K. W. Godfrey, Geometrical frustration in the ferromagnetic pyrochlore $Ho_2Ti_2O_7$, Phys. Rev. Lett. **79**, 2554 (1997).

[17] S. T. Bramwell and M. J. P. Gingras, Spin ice state in frustrated magnetic pyrochlore materials, Science **294**, 1495 (2001).

[18] S. M. Yan, D. A. Huse, and S. R. White, Spin-liquid ground state of the $S = 1/2$ kagome Heisenberg antiferromagnet, Science **332**, 1173 (2011).

[19] S. Depenbrock, I. P. McCulloch, and U. Schollwöck, Nature of the spin-liquid ground state of the $S = 1/2$ Heisenberg model on the kagome lattice, Phys. Rev. Lett. **109**, 067201 (2012).

[20] Y. Ran, M. Hermele, P. A. Lee, and X. G. Wen, Projected-wave-function study of the spin-1/2 Heisenberg model on the kagome lattice, Phys. Rev. Lett. **98**, 117205 (2007).

[21] M. Hermele, Y. Ran, P. A. Lee, and X. G. Wen, Properties of an algebraic spin liquid on the kagome lattice, Phys. Rev. B **77**, 224413 (2008).

[22] Y. Iqbal, F. Becca, and D. Poilblanc, Projected wave function study of Z_2 spin liquids on the kagome lattice for the spin-$\frac{1}{2}$ quantum Heisenberg antiferromagnet, Phys. Rev. B **84**, 020407(R) (2011).

[23] Y. C. He, M. P. Zaletel, M. Oshikawa, and F. Pollmann, Signatures of Dirac cones in a DMRG study of the kagome Heisenberg model, Phys. Rev. X **7**, 031020 (2017).

[24] X. Chen, S. J. Ran, T. Liu, C. Peng, Y. Z. Huang, and G. Su, Thermodynamics of spin-1/2 kagomé Heisenberg antiferromagnet: Algebraic paramagnetic liquid and finite-temperature phase diagram, Sci. Bull. **63**, 1545 (2018).

[25] M. P. Shores, E. A. Nytko, B. M. Bartlett, and D. G. Nocera, A structurally perfect $S = 1/2$ kagomé antiferromagnet, J. Am. Chem. Soc. **127**, 13462 (2005).

[26] J. S. Helton, K. Matan, M. P. Shores, E. A. Nytko, B. M. Bartlett, Y. Yoshida, Y. Takano, A. Suslov, Y. Qiu, J.-H. Chung, D. G. Nocera, and Y. S. Lee, Spin dynamics of the spin-1/2 kagome lattice antiferromagnet $ZnCu_3(OH)_6Cl_2$, Phys. Rev. Lett. **98**, 107204 (2007).

[27] A. Olariu, P. Mendels, F. Bert, F. Duc, J. C. Trombe, M. A. de Vries, and A. Harrison, ^{17}O NMR study of the intrinsic magnetic susceptibility and spin dynamics of the quantum kagome antiferromagnet $ZnCu_3(OH)_6Cl_2$, Phys. Rev. Lett. **100**, 087202 (2008).

[28] T. Imai, M. Fu, T. H. Han, and Y. S. Lee, Local spin susceptibility of the $S = \frac{1}{2}$ kagome lattice in $ZnCu_3(OD)_6Cl_2$, Phys. Rev. B **84**, 020411(R) (2011).

[29] J. M. Wang, W. S. Yuan, P. M. Singer, R. W. Smaha, W. He, J. J. Wen, Y. S. Lee, and T. Imai, Emergence of spin singlets with inhomogeneous gaps in the kagome lattice Heisenberg antiferromagnets Zn-barlowite and herbertsmithite, Nat. Phys. **17**, 1109 (2021).

[30] D. E. Freedman, T. H. Han, A. Prodi, P. Meller, Q. Z. Huang, Y. S. Chen, S. M. Webb, Y. S. Lee, T. M. McQueen, and D. G. Nocera, Site specific x-ray anomalous dispersion of the geometrically frustrated kagomé magnet, herbertsmithite, $ZnCu_3(OH)_6Cl_2$, J. Am. Chem. Soc. **132**, 16185 (2010).

[31] M. Jeong, F. Bert, P. Mendels, F. Duc, J. C. Trombe, M. A. de Vries, and A. Harrison, Field-induced freezing of a quantum spin liquid on the kagome lattice, Phys. Rev. Lett. **107**, 237201 (2011).

[32] P. Khuntia, M. Velazquez, Q. Barthlemy, F. Bert, E. Kermarrec, A. Legros, B. Bernu, L. Messio, A. Zorko, and P. Mendels, Gapless ground state in the archetypal quantum kagome antiferromagnet $ZnCu_3(OH)_6Cl_2$, Nat. Phys. **16**, 469 (2020).

[33] Y. Y. Huang, Y. Xu, L. Wang, C. C. Zhao, C. P. Tu, J. M. Ni, L. S. Wang, B. L. Pan, Y. Fu, Z. Y. Hao, C. Liu, J. W. Mei, and S. Y. Li, Heat transport in herbertsmithite: Can a quantum spin liquid survive disorder? Phys. Rev. Lett. **127**, 267202 (2021).

[34] J. M. Wang, W. S. Yuan, P. M. Singer, R. W. Smaha, W. He, J. J. Wen, Y. S. Lee, and T. Imai, Freezing of the lattice in the kagome lattice Heisenberg antiferromagnet Zn-barlowite $ZnCu_3(OD)_6FBr$, Phys. Rev. Lett. **128**, 157202 (2022).

[35] D. S. Fisher, Random antiferromagnetic quantum spin chains, Phys. Rev. B **50**, 3799 (1994).

[36] R. R. P. Singh, Valence bond glass phase in dilute kagome antiferromagnets, Phys. Rev. Lett. **104**, 177203 (2010).

[37] W. Sun, Y. X. Huang, S. Nokhrin, Y. M. Pan, and J. X. Mi, Perfect kagomé lattices in $YCu_3(OH)_6Cl_3$: A new candidate for the quantum spin liquid state, J. Mater. Chem. C **4**, 8772 (2016).

[38] Q. Barthélemy, P. Puphal, K. M. Zoch, C. Krellner, H. Luetkens, C. Baines, D. Sheptyakov, E. Kermarrec, P. Mendels, and F. Bert, Local study of the insulating quantum kagome antiferromagnets $YCu_3(OH)_6O_xCl_{3-x}$ ($x = 0, 1/3$), Phys. Rev. Mater. **3**, 074401 (2019).

[39] T. Arh, M. Gomilšek, P. Prelovšek, M. Pregelj, M. Klanjšek, A. Ozarowski, S. J. Clark, T. Lancaster, W. Sun, J. X. Mi, and A. Zorko, Origin of magnetic ordering in a structurally perfect quantum kagome antiferromagnet, Phys. Rev. Lett. **125**, 027203 (2020).

[40] J. Wang, M. Spitaler, Y.-S. Su, K.M. Zoch, C. Krellner, P. Puphal, S.E. Brown, and A. Pustogow, Controlled frustration release on the kagome lattice by uniaxial-strain tuning, Phys. Rev. Lett. **131**, 256501 (2023).

[41] M. Hering, F. Ferrari, A. Razpopov, I. I. Mazin, R. Valentí, H. O. Jeschke, and J. Reuther, Phase diagram of a distorted kagome antiferromagnet and application to Y-kapellasite, npj Comput. Mater. **8**, 10 (2022).

[42] D. Chatterjee, P. Puphal, Q. Barthélemy, J. Willwater, S. Süllow, C. Baines, S. Petit, E. Ressouche, J. Ollivier, K. M. Zoch, C. Krellner, M. Parzer, A. Riss, F. Garmroudi, A. Pustogow, P. Mendels, E. Kermarrec, and F. Bert, From spin liquid to magnetic ordering in the anisotropic kagome Y-kapellasite $Y_3Cu_9(OH)_{19}Cl_8$: A single-crystal study, Phys. Rev. B **107**, 125156 (2023).

[43] P. Puphal, M. Bolte, D. Sheptyakov, A. Pustogow, K. Kliemt, M. Dressel, M. Baenitz, and C. Krellner, Strong magnetic frustration in $Y_3Cu_9(OH)_{19}Cl_8$: A distorted kagomé antiferromagnet, J. Mater. Chem. C **5**, 2629 (2017).

[44] X. H. Chen, Y. X. Huang, Y. Pan, and J. X. Mi, Quantum spin liquid candidate $YCu_3(OH)_6Br_2[Br_x(OH)_{1-x}]$ ($x = 0.51$): With an almost perfect kagome layer, J. Magn. Magn. Mater. **512**, 167066 (2020).

[45] J. B. Liu, L. Yuan, X. Li, B. Q. Li, K. Zhao, H. J. Liao, and Y. S. Li, Gapless spin liquid behavior in a kagome Heisenberg

antiferromagnet with randomly distributed hexagons of alternate bonds, Phys. Rev. B **105**, 024418 (2022).

[46] Z. Y. Zeng, X. Y. Ma, S. Wu, H. F. Li, Z. Tao, X. Y. Lu, X. H. Chen, J. X. Mi, S. J. Song, G. H. Cao, G. W. Che, K. Li, G. Li, H. Q. Luo, Z. Y. Meng, and S. L. Li, Possible Dirac quantum spin liquid in the kagome quantum antiferromagnet $YCu_3(OH)_6Br_2[Br_x(OH)_{(1-x)}]$, Phys. Rev. B **105**, L121109 (2022).

[47] F. J. Lu, L. Yuan, J. Zhang, B. Q. Li, Y. K. Luo, and Y. S. Li, The observation of quantum fluctuations in a kagome Heisenberg antiferromagnet, Commun. Phys. **5**, 272 (2022).

[48] X. C. Hong, M. Behnami, L. Yuan, B. Q. Li, W. Brenig, B. Büchner, Y. S. Li, and C. Hess, Heat transport of the kagome Heisenberg quantum spin liquid candidate $YCu_3(OH)_{6.5}Br_{2.5}$: Localized magnetic excitations and a putative spin gap, Phys. Rev. B **106**, L220406 (2022).

[49] Detailed theoretical calculations, the fitting of ν_Q, NQR spectra, and spin recovery curves are included in the Supplemental Material at http://link.aps.org/supplemental/10.1103/PhysRevB.109.104403.

[50] Z. Y. Zeng, C. K. Zhou, H. L. Zhou, L. K. Han, R. Z. Chi, K. Li, M. Kofu, K. Nakajima, Y. Wei, W. L. Zhang, D. G. Mazzone, Z. Y. Meng, and S. L. Li, Dirac quantum spin liquid emerging in a kagome-lattice antiferromagnet, arXiv:2310.11646.

[51] R.-Y. Sun, Z. Zhu, and Z.-Y. Weng, Localization in a t-J-type model with translational symmetry, Phys. Rev. Lett. **123**, 016601 (2019).

[52] Z. Zhu, H. C. Jiang, Y. Qi, C. Tian, and Z. Y. Weng, Strong correlation induced charge localization in antiferromagnets, Sci. Rep. **3**, 2586 (2013).

[53] G. X. Zheng, Y. Zhu, K. W. Chen, B. Kang, D. Zhang, K. Jenkins, A. Chan, Z. Y. Zeng, A. N. Xu, O. A. Valenzuela, J. Blawat, J. Singleton, P. A. Lee, S. L. Li, and L. Li, Unconventional magnetic oscillations in kagome Mott insulators, arXiv:2310.07989.

[54] A. Zorko, M. Pregelj, M. Klanjšek, M. Gomilšek, Z. Jagličić, J. S. Lord, J. A. T. Verezhak, T. Shang, W. Sun, and J. X. Mi, Coexistence of magnetic order and persistent spin dynamics in a quantum kagome antiferromagnet with no intersite mixing, Phys. Rev. B **99**, 214441 (2019).

[55] A. Zorko, M. Pregelj, M. Gomilšek, M. Klanjšek, O. Zaharko, W. Sun, and J. X. Mi, Negative-vector-chirality 120° spin structure in the defect- and distortion-free quantum kagome antiferromagnet $YCu_3(OH)_6Cl_3$, Phys. Rev. B **100**, 144420 (2019).